Supporting Information for "Focused mid-crustal magma intrusion during continental break-up in Ethiopia"

Kevin Wong[1], David Ferguson[1], Penny Wieser[2], Daniel Morgan[1], Marie Edmonds[3], Amdemichael Zafu Tadesse[4], Gezahegn Yirgu[5], Jason Harvey[1], and Samantha Hammond[6]

[1]School of Earth and Environment, University of Leeds, Leeds LS2 9JT, United Kingdom

[2]Earth and Planetary Science, University of California, Berkeley, CA 94720-4767, United States of America

[3]Centre for the Observation and Modelling of Earthquakes, Volcanoes and Tectonics (COMET), Department of Earth Sciences, University of Cambridge, Cambridge CB2 3EQ, United Kingdom

[4]Department of Geosciences, Environment and Society, Université Libre de Bruxelles, 50 B-1050 Bruxelles, Belgium

[5]School of Earth Sciences, Addis Ababa University, P. O. Box 1176 Addis Ababa, Ethiopia

[6]School of Environment, Earth and Ecosystems Sciences, The Open University, Milton Keynes MK7 6AA, United Kingdom

Contents of this file

Corresponding author: K. Wong, Dipartimento di Scienze Biologiche, Geologiche, e Ambientali (BiGeA), Alma Mater Studiorum Università di Bologna, Piazza di Porta San Donato 1, 40126, Bologna, Italy (kevin.wong@unibo.it)

2. Table S1

3. Figures S1 to S9

Additional Supporting Information (Files uploaded separately)

1. Dataset S1: standards and geochemical analyses of melt inclusions, whole rocks, and carrier glasses.

2. Transmitted and reflected light microscope images of analysed melt inclusions.

Introduction

The Supplementary Information contains text (Text S1) detailing analytical methods, expanded Raman spectroscopy results, volatile solubility and melt fractionation modelling, and CO_2 flux estimation calculations. Text S1 is complemented by Figures S1 to S9, and Table S1.

Text S1.

1. Analytical methods

Data, standards, secondary standards, and the accuracy and precision of all analyses on Main Ethiopian Rift (MER) materials are provided in Dataset S1.

1.1. Raman spectroscopy

Olivines hosting melt inclusions were picked from scoria from the two Boku Volcanic Complex localities shown in Figure 1 in the main text, and mounted onto glass slides using CrystalBond^{TM}. Crystals hosting melt inclusions with shrinkage bubbles were ground down until melt inclusions were within ∼100 μm of the surface, and then polished to 1 μm grade using silicon carbide papers and diamond pastes. Transmitted light optical microscopy was used to obtain high quality imagery of the melt inclusion and bubble. The outline of the bubble and melt inclusion were traced and fitted with ellipses using ImageJ to obtain dimensions for each (Schneider et al., 2012). Volumes of bubbles and melt inclusions were calculated assuming that the non-measurable dimension (orthogonal to the plane of polishing) was equal to the arithmetic mean of the two dimensions that could be measured. This introduces a 1σ error of +37/-47 % (Tucker et al., 2019), which dwarfs other uncertainties from Raman spectroscopy.

CO_2 densimetry of melt inclusion vapor bubbles was performed using the confocal Horiba LabRAM 300 Raman spectrometer at the Department of Earth Sciences, University of Cambridge over five days in February 2020, using a 100 mW 532.05 nm Ventus laser source focussed on the sample with an Olympus LMPLFLN 50× working distance objective lens. Spectra were collected with a Peltier front-illuminated 1024×256 pixel

CCD detector with a holographic grating of 1800 gr/mm, a confocal aperture of 300 *mu*m, and a slit width of 100 *mu*m. Our analyses were performed at room temperature, and only CO_2 in the vapor bubble was considered in the Raman spectrum. The instrument was calibrated at the start of every day using the Labspec 6 autocalibration function, which assesses the linearity of the spectrum relative to the Si peak between 0 and 520.69 cm^{-1}. Spectra were collected within a single spectral window centered on 1250 cm^{-1}. Fermi diads obtained from Raman spectroscopy were fitted with Gaussian peaks after correcting for a fourth-order polynomial-fitted background, and diad splitting (Δ, in cm^{-1}) was determined through the difference of the means of the peaks. The relationship between diad splitting and CO_2 density (ρCO_2, in g cm^{-3}) has been previously assessed for this machine by Wieser et al. (2021) owing for the necessity of calibrating each individual Raman machine (Lamadrid et al., 2017), and takes the form of the following linear relation:

$$\rho_{CO_2} = 0.3217\Delta - 32.9955 \tag{1}$$

The density of CO_2 in the bubble is converted into concentration through mass balance (Hartley et al., 2014):

$$[CO_2] = 10^6 \times \frac{\rho_{CO_2} \cdot V_{VB}}{\rho_{melt} \cdot V_{MI}} \tag{2}$$

where V_{VB} and V_{MI} are the volume of the vapor bubble and the melt inclusion glass respectively, and $\rho_{melt} = 2.706$ g cm^{-3} is the mean density of our melt inclusions determined using the software DensityX (Iacovino & Till, 2019). The total concentration of

CO_2 within the melt inclusion is then simply the sum of the CO_2 concentration in the bubble and the CO_2 concentration of the melt inclusion glass, which is assessed using SIMS (Supplement Section 2).

Removal of artifacts in the Raman spectrum was accomplished through multiple accumulations (5×60 s). Where signal strength of the Fermi diad was weak, longer count times were used at the expense of the number of accumulations (4×90 s). Each sample was run three times to obtain a mean and standard deviation; clear anomalies were not considered when computing the mean.

In addition to primary calibration performed every morning on a Si chip, secondary standards were measured at regular intervals throughout the day to check for instrument drift. The secondary standard used is a synthetic quartz-hosted fluid inclusion (label E) calibrated using an optical cell. Figure S1 shows repeat measurements of the Raman instrument over the course of a day, for five days. Precision in measuring bubble density was 5.8 %, and the accuracy relative to the mean diad splitting of (Wieser et al., 2021) was 0.9 %. Secondary standards were run with a shorter analysis time of 4×30 second accumulations as CO_2 diad signals were typically stronger than those of the samples. As with the samples, each secondary standard acquisition was measured three times to obtain a mean and standard deviation of repeat analyses. Mean peak splitting of the secondary standard appeared to be affected by instrument drift on some days (Figure S1); whether this results from temperature effects remains uncertain and should be explored in future studies using this Raman spectrometer. A linear correction was applied to data collected during the days where this effect is most prominent (12/02/2020 and 14/02/2020).

Dimensions of melt inclusions, their bubbles, and diad splitting are provided in Supplementary Dataset S1. All melt inclusion shrinkage bubbles analyzed for CO_2 returned a Fermi diad. ∼35 % of bubbles produce Fermi diads with splittings corresponding to densities >0.20 g cm^{-3}. At room temperature, bubbles with densities greater than >∼0.20–0.23 g cm^{-3} (depending on the exact temperature of the room and any heating from the laser) will consist of a vapor phase in the center with a density of 0.20–0.23 g cm^{-3} and a liquid CO_2 phase on the walls with a density of ∼0.7 g cm^{-3}. The fact that we measure some densities above ∼0.23 g cm^{-3} could represent analytical error; repeated measurements yielded standard deviations of ∼0.04 cm^{-1} in diad splitting corresponding to standard deviations in density of ∼0.01 g cm^{-3}; warmer room temperatures and small amounts of laser heating are also expected. As our bubbles were not heated above the critical point of CO_2 where a single phase is measured, our Raman measurements which only measure the interior vapor phase will underestimate the true density of the bubble (e.g., Moore et al., 2018). We do not observe any liquid films or 'bouncing bubbles': where the liquid phase is abundant enough Brownian motion causes the interior bubble to bounce. The absence of this motion suggests that if a liquid film were present, it is likely thin, so our measurements do not represent substantial underestimates.

∼15 % of the shrinkage bubble Raman spectra contain a noticeable carbonate signature (∼1090 cm^{-1}, see Figure S2; Moore et al., 2015; DeVitre et al., 2021). Only one bubble had a strong Raman carbonate signal, whereas the majority of carbonate signals were comparatively weak (Figure S2); we therefore believe that the presence of carbonate in MER melt inclusion shrinkage bubbles is fairly uncommon, and concentrations of carbon-

ate are low when present. Owing to the overlap in CO_2 densities between bubbles that do and do not return a carbonate signature, we believe that the effect of sequestration of CO2 within carbonate is within uncertainty.

1.2. Secondary ion mass spectrometry (SIMS)

Crystals both with and without shrinkage bubbles were ground down to expose the melt inclusions. By doing so, most shrinkage bubbles were ruptured. The crystals were then mounted in epoxy blocks, and polished with progressively finer diamond pastes (culminating in 0.25 μm grade paste). In between each step of polishing the epoxy blocks were thoroughly cleaned through ultrasonication.

Volatile element and selected trace element concentrations were determined by secondary ion mass spectrometry (SIMS). The final stages of sample preparation and the SIMS analyses themselves were performed by Dr. Cristina Talavera Rodriguez using the Cameca IMS-7f-Geo at the NERC Ion Microprobe Facility, University of Edinburgh, owing to the COVID-19 pandemic. A gold coat was applied to the epoxy blocks, which were subsequently placed in the sample chamber at vacuum for several hours to allow for outgassing prior to the start of the analyses. SIMS was performed using a 5-6 nA 15 m diameter oval beam of O^- ions with an acceleration voltage of 13 kV. Positive secondary ions were accelerated to 5000 eV, with an offset of -50 eV for ^{12}C and -75 eV for ^{1}H and trace elements.

$^{26}Mg^+$, $^{30}Si^+$, $^{40}Ca^{2+}$, $^{85}Rb^+$, $^{88}Sr^+$, $^{89}Y^+$, $^{138}Ba^+$, $^{139}La^+$, and $^{140}Ce^+$ were counted for 2 seconds; $^{7}Li^+$ was counted for 3 seconds; $^{1}H^+$, $^{24}Mg^{2+}$, $^{93}Nb^+$, $^{141}Pr^+$, $^{143}Nd^+$, $^{157}Gd^+$, $^{159}Tb^+$, and $^{161}Dy^+$ were counted for 5 seconds; $^{149}Sm^+$, $^{171}Yb^+$, and $^{175}Lu^+$ were counted

for 8 seconds; $^{12}C^{+}$ and $^{19}F^{+}$ were counted for 10 seconds. Counts were then normalized to 30Si and converted into concentrations. For C, 15 scans were performed, but only the last 8 were used to avoid surface contamination at the beginning of each analysis and to allow the C signal to stabilize. Similarly, 20 scans were performed for H from which the last 10 were used. As the ion yield of these two elements correlate with SiO_2, calibration curves were determined using a range of standards of variable SiO_2 (M40, N72, M36, M21, M5, M10, M47; Figure S3; Hauri et al., 2002; Shishkina et al., 2010). A background correction was applied by removing the number of counts for C and H_2O recorded by the CO_2- and H_2O-free standard N72 (Shishkina et al., 2010). General calibration was performed in every session using MPI-DING glasses (GSD-1, NIST610, KL2-G, ML3B; Jochum et al., 2006).

1.3. Electron probe microanalysis (EPMA)

Following SIMS analyses the gold coat was removed by polishing each epoxy block with 0.25 μm grade diamond paste for 2 minutes, and a carbon coat was applied for electron probe microanalysis (EPMA). Analyses to determine major element concentrations were performed on melt inclusions, matrix glasses, and host olivines using the JEOL JXA8230 at Leeds Electron Microscopy and Spectroscopy Centre (LEMAS), University of Leeds. Olivine analyses were performed using a 40 nA beam with 20 kV acceleration voltage; glass analyses, including both melt inclusions and carrier glasses, were performed using a defocused 5 μm beam with 15 kV acceleration voltage, with beam currents of 6 nA for Na and K and 15 nA for all other major elements. Spectrometer configurations, count times, calibration materials, and estimates of precision and accuracy from secondary standard

analyses (olivine: San Carlos Olivine NMNH 111312-44; Jarosewich (2002); basaltic glass: ML3-B and KL2-G; Jochum et al. (2006)) are included in Supplementary Dataset S1. Data reduction is performed using the ProbeForEPMA software (Donovan, 2021).

1.4. Post-entrapment crystallization corrections

Melt inclusion post-entrapment crystallization and Fe-loss was corrected using Petrolog3 (Danyushevsky & Plechov, 2011). Initial FeO_t was set at 12.69 wt%, which is the mean FeO_t of carrier glasses from the Boku Volcanic Complex (see Supplementary Dataset S1). The olivine-melt model selected was (Danyushevsky, 2001), and the QFM buffer was chosen for the oxidation state (Gleeson et al., 2017). Changing the initial FeO_t by 1.5 wt% affects MagmaSat pressures by a mean of 8±4 %, which does not significantly influence the results of this study.

1.5. X-ray fluorescence

A subset of scoria samples from cones in the Boku Volcanic Complex were powdered using an agate ball mill at the University of Leeds to 150 μm grade. X-ray fluorescence was performed using the Rigaku ZSX Primus WDXRF at the University of Leeds by Lesley Neve. Prior to analyses all samples were dried at 105 °C to remove remaining moisture. Loss on ignition was assessed at 1025 °C for at least one hour. A 1:10 ratio of sample:flux (comprising 66 % $Li_2B_4O_7$ and 34 % $LiBO_2$) supplemented with 3 drops of LiI was used to create fused beads. Sample-flux mixtures were cast at 1150 ∘C for 20 minutes in platinum crucibles to allow for the sample to dissolve. Once molten, the beads were allowed to cool to room temperature and cleaned with 25 % HCl. The standards USGS BCR-1 and STSD-4 were run at the start of the session and at regular intervals

throughout. Detection limits were 0.03 wt% for MgO and Na2O, and 0.01 wt% for all other elements.

1.6. Solution ICP-MS

The samples powdered for XRF were digested in strong ultrapure acids (Romil UpA). Solution ICP-MS was performed using the Agilent 8800 QQQ at the Open University. To correct for plasma fractionation and drift, samples were run with internal standards (Be, Rh, In, Tm and Bi) bled in at the same time. Calibration standards were run at the start of the analytical period, followed by the samples. BHVO-2, JP-1, and WSE were analyzed as secondary standards. Monitors were analyzed every 5 unknowns to check for instrument drift. Detection limits were at most 0.012 μg g^{-1}.

2. Raman spectroscopy results

76 melt inclusion shrinkage bubbles analyzed by Raman spectroscopy returned a Fermi diad (Supplementary Dataset S1). Bubble CO_2 densities range from 0.12 to 0.27 g cm^{-3}, with a mean density of 0.19 g cm^{-3} (Figure S3), in excess of the expected detection limit for the Raman machine used (0.02 g cm^{-3} Wieser et al., 2021). Vapor bubbles constitute 0.09 to 2.85 vol% of the melt inclusion, and are similar in vol% to bubbles from Iceland (Hartley et al., 2014).

As shown in Figure S4 there are no clear correlations between bubble CO_2 density and melt inclusion volume (Figure S4A), bubble volume (Figure S4B), or bubble volume proportion of the melt inclusion (Figure S4C). Furthermore, in the samples where SIMS and subsequent EPMA has been performed, there is no correlation between bubble volume proportion and PEC as observed in melt inclusions from Hawaii (Wieser et al., 2021). No

difference in bubble densities or melt inclusion and bubble dimensions were observed between the two cones sampled in our study.

2.1. Corrections for empty bubbles

Although 76 melt inclusion shrinkage bubbles were analyzed by Raman spectroscopy, a significant number could not be analyzed by SIMS owing to their small size. The melt inclusions considered in the main text of this study are therefore a mixture of samples that have been analyzed by Raman and others which were not, but were selected owing to their size. Several melt inclusions therefore have shrinkage bubbles that were not analyzed by Raman prior to SIMS.

We consider pressures from total CO_2 from these melt inclusions, assuming that their bubbles have CO_2 densities of 0.21 g cm^{-3}. This density falls near the mean of all melt inclusion vapor bubbles (0.18 g cm^{-3}), and could correspond to the maximum possible CO_2 vapor density below the critical point (DeVitre et al., 2022). We apply this maximum density with post-rupture measurements of the bubble to estimate total melt inclusion CO_2.

Nine melt inclusions are corrected in this manner, and seven are shown in Figure 2 of the main text as green diamonds with a trail leading to the pressure corresponding to the maximum vapor bubble CO_2 density. These seven inclusions have maximum pressures within the range 8–18 km, in agreement with our proposed focused intrusion zone of 10–15 km.

The remaining two melt inclusions, already recording the highest CO_2 in the dataset from glass analyses only, return maximum possible pressures nearing 10 kbar if bubble

CO_2 is estimated, i.e., under the MER crust and within the lithospheric mantle. For these two melt inclusions the bubble constitutes 6.5 vol% of the overall melt inclusion volume and make up more than twice the volume percentage of all other melt inclusion shrinkage bubbles (Figure S5). These samples may have significantly degassed, and may have been derived from deepest parts of the sub-rift magmatic system; these inclusions may also have co-entrapped magmatic bubbles and may not be suitable for estimating saturation pressures (e.g., Tucker et al., 2019). Tucker et al. (2019) note that one cannot differentiate between ensnared magmatic vapor bubbles and shrinkage bubbles that form after inclusion formation; in this study we err on the side of caution and do not estimate the pressures of these bubbles and inclusions in Figure 2 of the main text owing to their anomalous size relative to the other bubbles.

3. Volatile solubility modelling

The open-source Python 3 library VESIcal was used to determine volatile saturation pressures (Iacovino et al., 2021; Wieser et al., 2022), using the MagmaSat volatile saturation model (Ghiorso & Gualda, 2015). VESIcal models were run at a temperature of 1200 ∘C (Gleeson et al., 2017; Iddon et al., 2019; Wong et al., 2022) for all PEC-corrected melt inclusions in this study and for melt inclusions in Iddon and Edmonds (2020), assuming that PEC correction for this dataset was not necessary owing to the low reported PEC (<5 %). Uncertainties for volatile saturation pressure were determined using minimum and maximum CO_2 expected from 1σ melt inclusion volume uncertainty, which is the most significant uncertainty in our analyses. As shown in Figure S6, the primary control on determining saturation pressures for our melt inclusions using MagmaSat is CO_2 con-

centration. H_2O in our basaltic melt inclusions remains constant at 1.1±0.2 wt% up to ∼2 kbar (Figure S6).

Other saturation models have been calibrated for the composition and pressure ranges which our basaltic samples occupy. Figure S7 shows a comparison of MagmaSat compared to other basalt saturation models which are calibrated for our melt inclusion compositional range (Dixon, 1997; Shishkina et al., 2010; Iacono-Marziano et al., 2012; Allison et al., 2019). Both the Etna and Sunset Crater models of Allison et al. (2019) are selected owing to the broad calibration range of the former and the similarity in composition to our samples of the latter. For the majority of our melt inclusions the difference between a selected model and MagmaSat is typically less than 500 bars (∼2 km; see Figure S7). Kolmogotov-Smirnov statistics and p-values are presented in Table S1.

Entrapment pressures for melt inclusions calculated using MagmaSat and the models of Shishkina et al. (2010), Iacono-Marziano et al. (2012) and the Sunset Crater model of Allison et al. (2019) are statistically indistinguishable using Kolmogotov-Smirnov statistics at p=0.05 (Table S1). Owing to the compositional difference between our samples and the Etna basalt, the Allison et al. (2019) Etna model substantially underestimates pressures relative to other models (p <0.05 for all models except for Dixon, 1997, Table S1). Our samples fall on the North Arch Glasses regression line used to calibrate Dixon (1997) (and by extension the VolatileCalc model implemented in VESIcal; Newman & Lowenstern, 2002), and are therefore compositionally suitable for this solubility model. However, it has previously been suggested that this model is appropriate only for low H_2O and CO_2 contents and therefore low pressures (<1000 bar; Iacono-Marziano et al.,

2012). As the majority of our melt inclusions are likely to be entrapped at mid-crustal depths, the model of Dixon (1997) is deemed inappropriate for this work. The differences between MagmaSat and the other empirical models of volatile saturation are statistically insignificant and our samples are expected to have fractionated within their calibrated temperature and pressure ranges (Figure S7). These other models typically fall within the uncertainty envelope of melt inclusion and bubble volumes. We therefore favor the fully thermodynamic parameterisation of MagmaSat over the other empirical models.

4. Fractionation models

Liquid lines of descent for major elements were predicted using RhyoliteMELTS v1.2.0 (Gualda et al., 2012), using the three most primitive melt inclusion compositions as starting compositions. Models were run at an oxygen fugacity range of QFM-2 to QFM+1, which is characteristic of MER basalts (e.g., Gleeson et al., 2017). Pressures of fractionation of 2–4 kbars were selected based on the pressures obtained from VESIcal for melt inclusions for which total CO_2 was determined (see above). Model differences arising from starting oxygen fugacity and pressure were minor and are therefore not considered further. Trace element partitioning was modeled using the Rayleigh fractionation equation:

$$C = C_0 \cdot F^{(D-1)} \tag{3}$$

Where C_0 is the original concentration of an element, F is the melt fraction, and D is the bulk mineral-melt distribution coefficient. Melt fraction and mass proportions of olivine, clinopyroxene and plagioclase feldspar were determined from RhyoliteMELTS outputs; other mineral fractions were typically <5 wt% and hence were not considered.

Mineral-melt distribution coefficients were collated from Neave, Fabbro, Herd, Petrone, and Edmonds (2012) and Iddon and Edmonds (2020), and, other than Ba and Sr in plagioclase, were assumed to be constant. Distribution coefficients for Ba and Sr in plagioclase were calculated using the temperature-dependent partitioning of Blundy and Wood (1991).

5. CO_2 flux estimates

To estimate CO_2 fluxes resulting from the degassing of our melt inclusions, we estimate the quantity of melts supplied to the MER. The length of the MER is ∼1000 km, and the full spreading rate is ∼5.0 mm yr^{-1} (Saria et al., 2014). Assuming a melt density of 2700 kg m^{-3} (calculated as our mean melt inclusion density using DensityX; Iacovino & Till, 2019), and that the CO_2 degassed at mid-crustal pressures is 2.0±0.6 wt% (assuming same CO_2/Ba as MORB; Le Voyer et al., 2018), we consider three possible estimates of intruded melt thickness per unit of rift length:

• Firstly, we can assume that all new rifting crust is igneous; this is a suitable estimate as most present-day extension in the MER is predominantly magma-assisted (e.g., Kendall et al., 2005; Bastow et al., 2010). Using a crustal thickness of 28 km (Lavayssière et al., 2018), we estimate melt volume flux as 0.14 km^3 yr^{-1}, and a CO_2 flux of 7.6±2.7 Mt CO_2 yr^{-1}.

• Secondly, we can assume that 50% of extension in the MER is accommodated by magmatic intrusion (Daniels et al., 2014). If this is the case, melt volume flux and CO_2 flux are simply half that of the previous case: 0.07 km^3 yr^{-1} and 3.8±1.1 Mt CO_2 yr^{-1} respectively.

• Finally, we can calculate the proportion of igneous crust in rifting crust by comparing crustal thicknesses expected from stretching factors to present-day MER crustal thickness (Armitage et al., 2015; Wong et al., 2022). Using an intruded melt thickness of 3–6 km calculated from an estimated MER stretch factor of 1.2–1.5 (Wong et al., 2022), performing the calculations as above provides melt volume flux estimates of 0.02–0.03 $km^3\ y^{-1}$, and corresponding CO_2 flux estimates of 0.8±0.2 Mt $CO_2\ yr^{-1}$ (assuming 3 km), 1.2±0.4 Mt $CO_2\ yr^{-1}$ (assuming 4.5 km), and 1.6±0.5 Mt $CO_2\ yr^{-1}$ (assuming 6 km).

Our melt volume flux estimates, ranging from 0.02 to 0.14 $km^3\ yr^{-1}$, are similar to the range estimated by Iddon and Edmonds (2020). Similarly, our CO_2 flux estimates, which range from 0.8 to 7.6 Mt $CO_2\ yr^{-1}$, are of a similar magnitude to total CO_2 emissions of 0.52–4.36 Mt $CO_2\ yr^{-1}$ recorded by Hunt, Zafu, Mather, Pyle, and Barry (2017). We conclude therefore that the degassing of mid-crustal sill complexes can supply sufficient CO_2 to match the quantity degassed at geothermal centers in the MER.

References

Allison, C. M., Roggensack, K., & Clarke, A. B. (2019, June). H_2O–CO_2 solubility in alkali-rich mafic magmas: new experiments at mid-crustal pressures. *Contributions to Mineralogy and Petrology*, *174*(7), 58. Retrieved 2022-02-01, from `https://doi.org/10.1007/s00410-019-1592-4` doi: 10.1007/s00410-019-1592-4

Armitage, J. J., Ferguson, D. J., Goes, S., Hammond, J. O. S., Calais, E., Rychert, C. A., & Harmon, N. (2015, May). Upper mantle temperature and the onset of extension and break-up in Afar, Africa. *Earth and Planetary Science Letters*, *418*, 78–90. Re-

trieved 2018-10-03, from http://www.sciencedirect.com/science/article/pii/S0012821X15001259 doi: 10.1016/j.epsl.2015.02.039

Bastow, I. D., Pilidou, S., Kendall, J.-M., & Stuart, G. W. (2010, June). Melt-induced seismic anisotropy and magma assisted rifting in Ethiopia: Evidence from surface waves. *Geochemistry, Geophysics, Geosystems*, *11*(6). Retrieved 2018-11-02, from https://agupubs.onlinelibrary.wiley.com/doi/full/10.1029/2010GC003036 doi: 10.1029/2010GC003036

Blundy, J. D., & Wood, B. J. (1991, January). Crystal-chemical controls on the partitioning of Sr and Ba between plagioclase feldspar, silicate melts, and hydrothermal solutions. *Geochimica et Cosmochimica Acta*, *55*(1), 193–209. Retrieved 2017-05-25, from http://www.sciencedirect.com/science/article/pii/001670379190411W doi: 10.1016/0016-7037(91)90411-W

Daly, E., Keir, D., Ebinger, C. J., Stuart, G. W., Bastow, I. D., & Ayele, A. (2008, March). Crustal tomographic imaging of a transitional continental rift: The Ethiopian rift. *Geophysical Journal International*, *172*(3), 1033–1048. Retrieved 2018-11-01, from https://academic.oup.com/gji/article/172/3/1033/571185 doi: 10.1111/j.1365-246X.2007.03682.x

Daniels, K. A., Bastow, I. D., Keir, D., Sparks, R. S. J., & Menand, T. (2014, January). Thermal models of dyke intrusion during development of continent–ocean transition. *Earth and Planetary Science Letters*, *385*, 145–153. Retrieved 2018-11-22, from http://www.sciencedirect.com/science/article/pii/S0012821X13005293 doi: 10.1016/j.epsl.2013.09.018

Danyushevsky, L. V. (2001, October). The effect of small amounts of H_2O on crystallisation of mid-ocean ridge and backarc basin magmas. *Journal of Volcanology and Geothermal Research*, *110*(3), 265–280. Retrieved 2021-03-30, from https://www.sciencedirect.com/science/article/pii/S037702730100213X doi: 10.1016/S0377-0273(01)00213-X

Danyushevsky, L. V., & Plechov, P. (2011, July). Petrolog3: Integrated software for modeling crystallization processes. *Geochemistry, Geophysics, Geosystems*, *12*(7), Q07021. Retrieved 2017-12-02, from http://onlinelibrary.wiley.com/doi/10.1029/2011GC003516/abstract doi: 10.1029/2011GC003516

DeVitre, C. L., Barth, A., Gazel, E., Plank, T. A., & Ramalho, R. (2021, December). Solving the Carbonate Problem in Melt Inclusion Bubbles. In *AGU Fall Meeting Abstracts.* Retrieved from https://agu.confex.com/agu/fm21/meetingapp.cgi/Paper/845682

DeVitre, C. L., Dayton, K., Gazel, E., Barth, A., Plank, T. A., Pamukcu, A., ... Monteleone, B. (2022, July). Accounting for Multi-Phase Carbon in Melt Inclusion Bubbles. In *Goldschmidt Conference Abstracts.* Retrieved 2022-08-08, from https://conf.goldschmidt.info/goldschmidt/2022/meetingapp.cgi/Paper/12601

Dixon, J. E. (1997, April). Degassing of alkalic basalts. *American Mineralogist*, *82*(3-4), 368–378. Retrieved 2022-01-05, from https://pubs.geoscienceworld.org/ammin/article/82/3-4/368-378/43291 doi: 10.2138/am-1997-3-415

Donovan, J. J. (2021). *Probe for EPMA v. 13.0.5 User's Guide and Reference (Xtreme Edition).* Retrieved 2022-06-07, from https://probesoftware.com/download/

PROBEWIN.pdf

Ghiorso, M. S., & Gualda, G. A. R. (2015, June). An H_2O–CO_2 mixed fluid saturation model compatible with rhyolite-MELTS. *Contributions to Mineralogy and Petrology*, *169*(6), 53. Retrieved 2021-11-25, from https://doi.org/10.1007/s00410-015-1141-8 doi: 10.1007/s00410-015-1141-8

Gleeson, M. L. M., Stock, M. J., Pyle, D. M., Mather, T. A., Hutchison, W., Yirgu, G., & Wade, J. (2017, May). Constraining magma storage conditions at a restless volcano in the Main Ethiopian Rift using phase equilibria models. *Journal of Volcanology and Geothermal Research*, *337*, 44–61. Retrieved 2018-10-24, from http://www.sciencedirect.com/science/article/pii/S0377027316304383 doi: 10.1016/j.jvolgeores.2017.02.026

Gualda, G. A. R., Ghiorso, M. S., Lemons, R. V., & Carley, T. L. (2012, May). Rhyolite-MELTS: a Modified Calibration of MELTS Optimized for Silica-rich, Fluid-bearing Magmatic Systems. *Journal of Petrology*, *53*(5), 875–890. Retrieved 2021-03-24, from https://doi.org/10.1093/petrology/egr080 doi: 10.1093/petrology/egr080

Hartley, M. E., Maclennan, J., Edmonds, M., & Thordarson, T. (2014, May). Reconstructing the deep CO_2 degassing behaviour of large basaltic fissure eruptions. *Earth and Planetary Science Letters*, *393*, 120–131. Retrieved 2018-02-16, from http://www.sciencedirect.com/science/article/pii/S0012821X14001125 doi: 10.1016/j.epsl.2014.02.031

Hauri, E., Wang, J., Dixon, J. E., King, P. L., Mandeville, C., & Newman, S. (2002, March). SIMS analysis of volatiles in silicate glasses: 1. Calibration,

matrix effects and comparisons with FTIR. *Chemical Geology*, *183*(1), 99–114. Retrieved 2022-02-21, from https://www.sciencedirect.com/science/article/pii/S0009254101003758 doi: 10.1016/S0009-2541(01)00375-8

Hunt, J. A., Zafu, A., Mather, T. A., Pyle, D. M., & Barry, P. H. (2017, October). Spatially Variable CO_2 Degassing in the Main Ethiopian Rift: Implications for Magma Storage, Volatile Transport, and Rift-Related Emissions. *Geochemistry, Geophysics, Geosystems*, *18*(10), 3714–3737. Retrieved 2018-08-07, from https://agupubs.onlinelibrary.wiley.com/doi/abs/10.1002/2017GC006975 doi: 10.1002/2017GC006975

Iacono-Marziano, G., Morizet, Y., Le Trong, E., & Gaillard, F. (2012, November). New experimental data and semi-empirical parameterization of H_2O–CO_2 solubility in mafic melts. *Geochimica et Cosmochimica Acta*, *97*, 1–23. Retrieved 2020-02-17, from http://www.sciencedirect.com/science/article/pii/S0016703712004930 doi: 10.1016/j.gca.2012.08.035

Iacovino, K., Matthews, S., Wieser, P. E., Moore, G. M., & Bégué, F. (2021). VESIcal Part I: An Open-Source Thermodynamic Model Engine for Mixed Volatile (H_2O-CO_2) Solubility in Silicate Melts. *Earth and Space Science*, *8*(11), e2020EA001584. Retrieved 2021-11-16, from https://onlinelibrary.wiley.com/doi/abs/10.1029/2020EA001584 (_eprint: https://onlinelibrary.wiley.com/doi/pdf/10.1029/2020EA001584) doi: 10.1029/2020EA001584

Iacovino, K., & Till, C. B. (2019, February). DensityX: A program for calculating the

densities of magmatic liquids up to 1,627 °C and 30 kbar. *Volcanica*, *2*(1), 1–10. Retrieved 2021-03-04, from http://jvolcanica.org/ojs/index.php/volcanica/article/view/12 (Number: 1) doi: 10.30909/vol.02.01.0110

Iddon, F., & Edmonds, M. (2020). Volatile-Rich Magmas Distributed Through the Upper Crust in the Main Ethiopian Rift. *Geochemistry, Geophysics, Geosystems*, *21*(6), e2019–GC008904. Retrieved 2020-06-24, from https://agupubs.onlinelibrary.wiley.com/doi/abs/10.1029/2019GC008904 (_eprint: https://agupubs.onlinelibrary.wiley.com/doi/pdf/10.1029/2019GC008904) doi: 10.1029/2019GC008904

Iddon, F., Jackson, C., Hutchison, W., Fontijn, K., Pyle, D. M., Mather, T. A., ... Edmonds, M. (2019). Mixing and Crystal Scavenging in the Main Ethiopian Rift Revealed by Trace Element Systematics in Feldspars and Glasses. *Geochemistry, Geophysics, Geosystems*, *20*(1), 230–259. Retrieved 2019-10-02, from https://agupubs.onlinelibrary.wiley.com/doi/abs/10.1029/2018GC007836 doi: 10.1029/2018GC007836

Jarosewich, E. (2002). Smithsonian Microbeam Standards. *Journal of Research of the National Institute of Standards and Technology*, *107*(6), 681–685. Retrieved 2022-02-21, from https://www.ncbi.nlm.nih.gov/pmc/articles/PMC4863845/ doi: 10.6028/jres.107.054

Jochum, K. P., Stoll, B., Herwig, K., Willbold, M., Hofmann, A. W., Amini, M., ... Woodhead, J. D. (2006). MPI-DING reference glasses for in situ microanalysis: New reference values for element concentrations and isotope ratios. *Geo-*

chemistry, Geophysics, Geosystems, *7*(2). Retrieved 2021-06-15, from https://agupubs.onlinelibrary.wiley.com/doi/abs/10.1029/2005GC001060 (_eprint: https://agupubs.onlinelibrary.wiley.com/doi/pdf/10.1029/2005GC001060) doi: 10.1029/2005GC001060

Keir, D., Ebinger, C. J., Stuart, G. W., Daly, E., & Ayele, A. (2006, May). Strain accommodation by magmatism and faulting as rifting proceeds to breakup: Seismicity of the northern Ethiopian rift. *Journal of Geophysical Research: Solid Earth*, *111*(B5). Retrieved 2018-11-01, from https://agupubs.onlinelibrary.wiley.com/doi/full/10.1029/2005JB003748 doi: 10.1029/2005JB003748

Kendall, J.-M., Stuart, G. W., Ebinger, C. J., Bastow, I. D., & Keir, D. (2005, January). Magma-assisted rifting in Ethiopia. *Nature*, *433*(7022), 146–148. Retrieved 2018-04-11, from https://www.nature.com/articles/nature03161 doi: 10.1038/nature03161

Lamadrid, H., Moore, L., Moncada, D., Rimstidt, J., Burruss, R., & Bodnar, R. (2017, February). Reassessment of the Raman CO_2 densimeter. *Chemical Geology*, *450*, 210–222. Retrieved 2020-02-09, from https://linkinghub.elsevier.com/retrieve/pii/S0009254116306945 doi: 10.1016/j.chemgeo.2016.12.034

Lavayssière, A., Rychert, C., Harmon, N., Keir, D., Hammond, J. O. S., Kendall, J.-M., ... Leroy, S. (2018, October). Imaging Lithospheric Discontinuities Beneath the Northern East African Rift Using S-to-P Receiver Functions. *Geochemistry, Geophysics, Geosystems*. Retrieved 2018-11-19, from https://agupubs.onlinelibrary.wiley.com/doi/abs/10.1029/2018GC007463 doi: 10.1029/2018GC007463

Le Voyer, M., Hauri, E. H., Cottrell, E., Kelley, K. A., Salters, V. J. M., Langmuir, C. H., ... Füri, E. (2018). Carbon fluxes and primary magma CO_2 contents along the global mid-ocean ridge system. *Geochemistry, Geophysics, Geosystems*, *20*(3), 1387–1424. Retrieved 2018-12-03, from https://agupubs.onlinelibrary.wiley.com/doi/abs/10.1029/2018GC007630 doi: 10.1029/2018GC007630

Moore, L. R., Gazel, E., Tuohy, R., Lloyd, A. S., Esposito, R., Steele-MacInnis, M., ... Bodnar, R. J. (2015, April). Bubbles matter: An assessment of the contribution of vapor bubbles to melt inclusion volatile budgets. *American Mineralogist*, *100*(4), 806–823. Retrieved 2019-05-13, from https://pubs.geoscienceworld.org/ammin/article/100/4/806-823/40390 doi: 10.2138/am-2015-5036

Moore, L. R., Mironov, N., Portnyagin, M., Gazel, E., & Bodnar, R. J. (2018, June). Volatile contents of primitive bubble-bearing melt inclusions from Klyuchevskoy volcano, Kamchatka: Comparison of volatile contents determined by mass-balance versus experimental homogenization. *Journal of Volcanology and Geothermal Research*, *358*, 124–131. Retrieved 2022-08-25, from https://www.sciencedirect.com/science/article/pii/S0377027317306510 doi: 10.1016/j.jvolgeores.2018.03.007

Neave, D. A., Fabbro, G., Herd, R. A., Petrone, C. M., & Edmonds, M. (2012, March). Melting, Differentiation and Degassing at the Pantelleria Volcano, Italy. *Journal of Petrology*, *53*(3), 637–663. Retrieved 2019-02-05, from https://academic.oup.com/petrology/article/53/3/637/1613886 doi: 10.1093/petrology/egr074

Newman, S., & Lowenstern, J. B. (2002, June). VolatileCalc: a silicate melt–H_2O–CO_2 solution model written in Visual Basic for excel. *Computers & Geosciences*, *28*(5),

597–604. Retrieved 2021-02-01, from http://www.sciencedirect.com/science/article/pii/S0098300401000814 doi: 10.1016/S0098-3004(01)00081-4

Saria, E., Calais, E., Stamps, D. S., Delvaux, D., & Hartnady, C. J. H. (2014, March). Present-day kinematics of the East African Rift. *Journal of Geophysical Research: Solid Earth*, *119*(4), 3584–3600. Retrieved 2018-11-01, from https://agupubs.onlinelibrary.wiley.com/doi/full/10.1002/2013JB010901 doi: 10.1002/2013JB010901

Schneider, C. A., Rasband, W. S., & Eliceiri, K. W. (2012, July). NIH Image to ImageJ: 25 years of image analysis. *Nature Methods*, *9*(7), 671–675. Retrieved 2021-03-17, from https://www.nature.com/articles/nmeth.2089 (Number: 7 Publisher: Nature Publishing Group) doi: 10.1038/nmeth.2089

Shishkina, T., Botcharnikov, R., Holtz, F., Almeev, R., & Portnyagin, M. (2010, October). Solubility of H_2O- and CO_2-bearing fluids in tholeiitic basalts at pressures up to 500MPa. *Chemical Geology*, *277*(1-2), 115–125. Retrieved 2021-09-10, from https://linkinghub.elsevier.com/retrieve/pii/S0009254110002640 doi: 10.1016/j.chemgeo.2010.07.014

Tucker, J. M., Hauri, E. H., Pietruszka, A. J., Garcia, M. O., Marske, J. P., & Trusdell, F. A. (2019, June). A high carbon content of the Hawaiian mantle from olivine-hosted melt inclusions. *Geochimica et Cosmochimica Acta*, *254*, 156–172. Retrieved 2019-05-15, from http://www.sciencedirect.com/science/article/pii/S001670371930208X doi: 10.1016/j.gca.2019.04.001

Wieser, P. E., Iacovino, K., Matthews, S., Moore, G., & Allison, C. M. (2022). VESI-

cal: 2. A Critical Approach to Volatile Solubility Modeling Using an Open-Source Python3 Engine. *Earth and Space Science*, *9*(2), e2021EA001932. Retrieved 2022-07-14, from https://onlinelibrary.wiley.com/doi/abs/10.1029/2021EA001932 (_eprint: https://onlinelibrary.wiley.com/doi/pdf/10.1029/2021EA001932) doi: 10.1029/2021EA001932

Wieser, P. E., Lamadrid, H., Maclennan, J., Edmonds, M., Matthews, S., Iacovino, K., ... Ilyinskaya, E. (2021). Reconstructing Magma Storage Depths for the 2018 Kilauean Eruption From Melt Inclusion CO_2 Contents: The Importance of Vapor Bubbles. *Geochemistry, Geophysics, Geosystems*, *22*(2), e2020GC009364. Retrieved 2021-02-13, from https://agupubs.onlinelibrary.wiley.com/doi/abs/10.1029/2020GC009364 (_eprint: https://agupubs.onlinelibrary.wiley.com/doi/pdf/10.1029/2020GC009364) doi: https://doi.org/10.1029/2020GC009364

Wong, K., Ferguson, D., Matthews, S., Morgan, D., Tadesse, A. Z., Sinetebeb, Y., & Yirgu, G. (2022, November). Exploring rift geodynamics in Ethiopia through olivine-spinel Al-exchange thermometry and rare-earth element distributions. *Earth and Planetary Science Letters*, *597*, 117820. Retrieved 2022-09-23, from https://www.sciencedirect.com/science/article/pii/S0012821X22004563 doi: 10.1016/j.epsl.2022.117820

Table S1. Kolmogorov-Smirnov statistics and p-values (in brackets) for different solubility models applied to our melt inclusions (see also Figure S7). Abbreviations are as follows: I.-M.: Iacono-Marziano et al. (2012); Allison-E: Allison et al. (2019) Etna model; Allison-S: Allison et al. (2019) Sunset Crater model.

K-S stat. (p)	**MagmaSat**	**Dixon**	**I.-M.**	**Shishkina**	**Allison-E**
Dixon	0.33 (0.03)	-	-	-	-
Iacono-Marziano	0.15 (0.77)	0.25 (0.16)	-	-	-
Shishkina	0.18 (0.58)	0.40 ($3{\cdot}10^{-3}$)	0.23 (0.27)	-	-
Allison-E	0.40 ($3{\cdot}10^{-3}$)	0.23 (0.27)	0.38 ($6{\cdot}10^{-3}$)	0.55 ($7{\cdot}10^{-6}$)	-
Allison-S	0.08 (1.00)	0.33 (0.03)	0.18 (0.58)	0.15 (0.77)	0.40 ($3{\cdot}10^{-3}$)

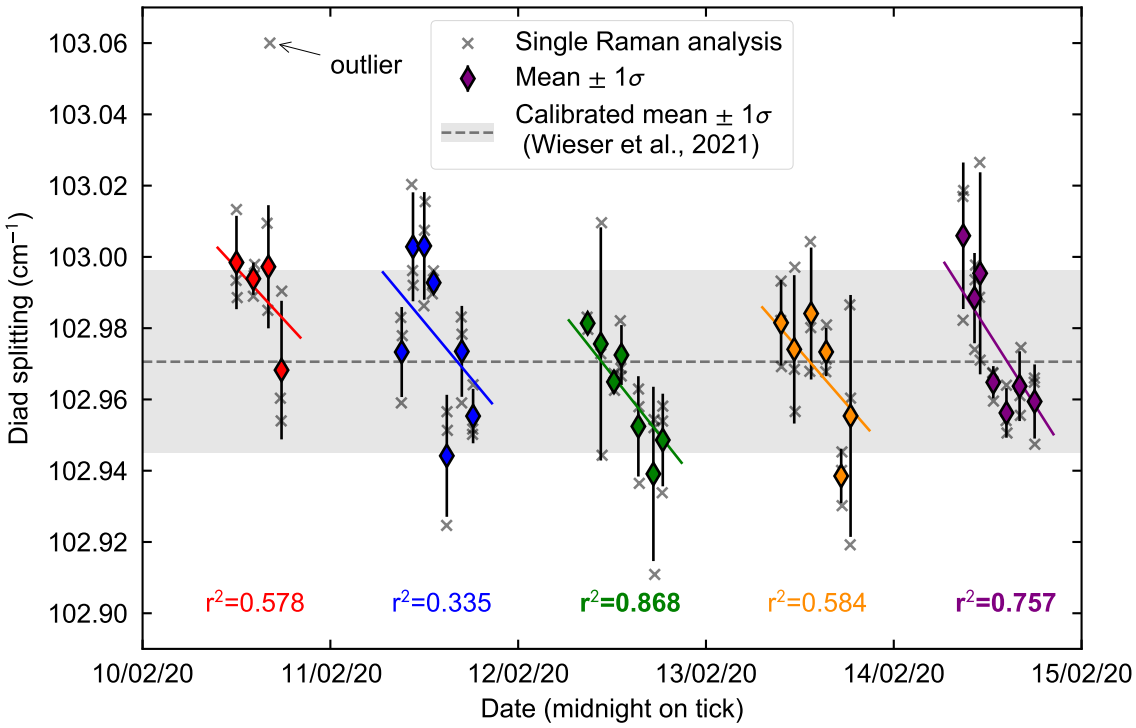

Figure S1. Secondary standard measurements on a synthetic quartz-hosted fluid inclusion used by (Wieser et al., 2021). Regression lines are fitted to analysis means.

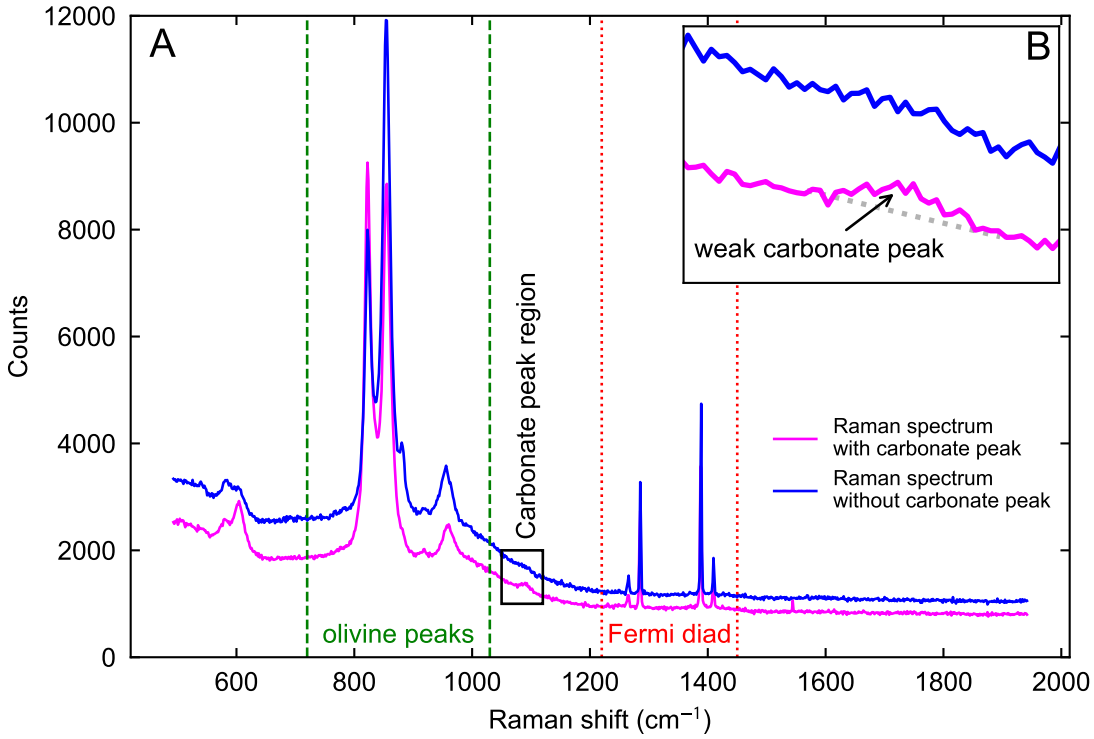

Figure S2. A. Raman spectra from this study with and without a carbonate peak at ∼1090 cm^{-1}. The region of the olivine peaks and Fermi diad are shown as the dashed and dotted regions respectively. B. Zoom inset on black rectangle in Subfigure A.

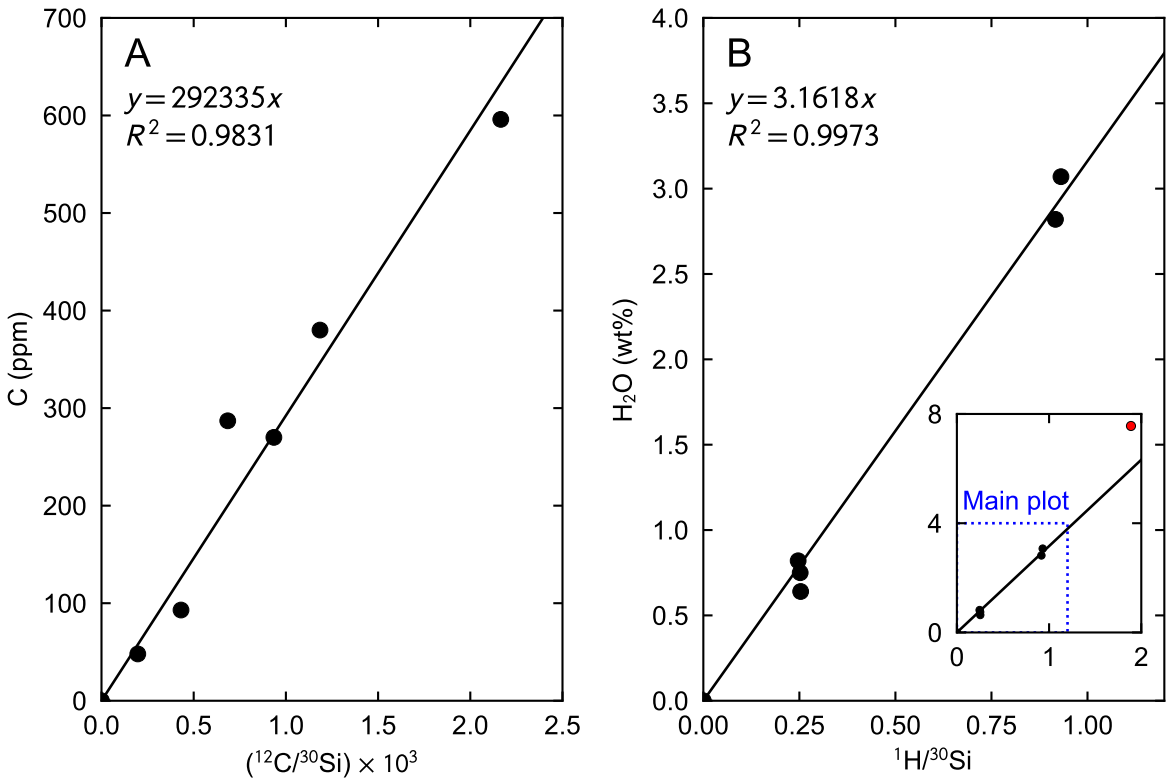

Figure S3. Calibration lines for basaltic standards used to convert measured counts of A) C and B) H_2O into concentrations. The subplot in subfigure B illustrates the position of the glass standard M21, which is shown as a red marker and was not used to determine the calibration line as its H2O concentration significantly exceeded those within our samples.

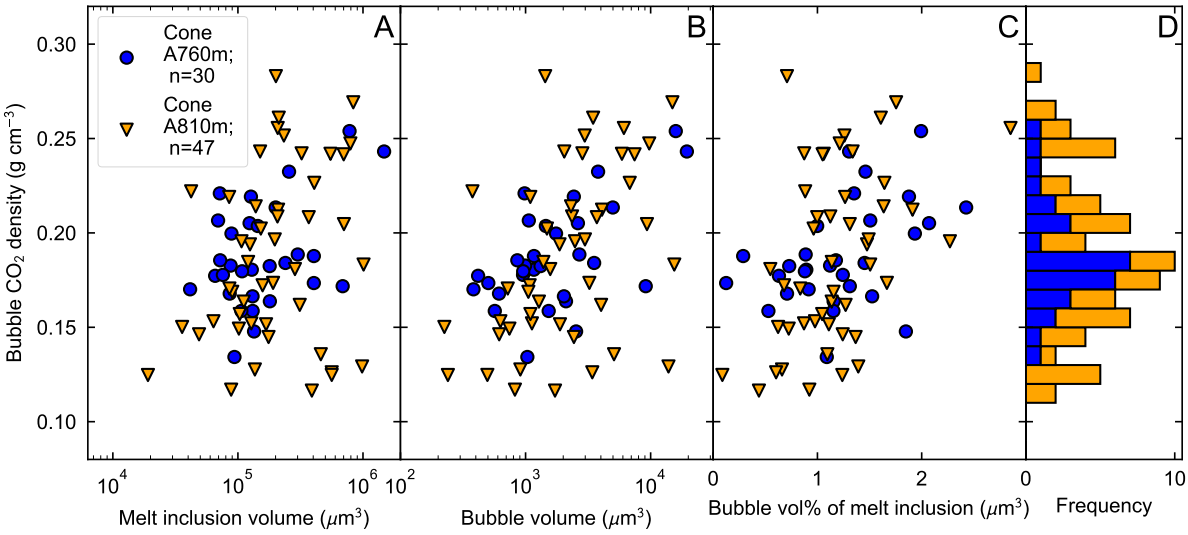

Figure S4. Bubble CO_2 density plotted against A. volume of melt inclusions, B. volume of shrinkage bubbles, C. bubble volume percentage of melt inclusions. D. Histogram of bubble CO_2 density.

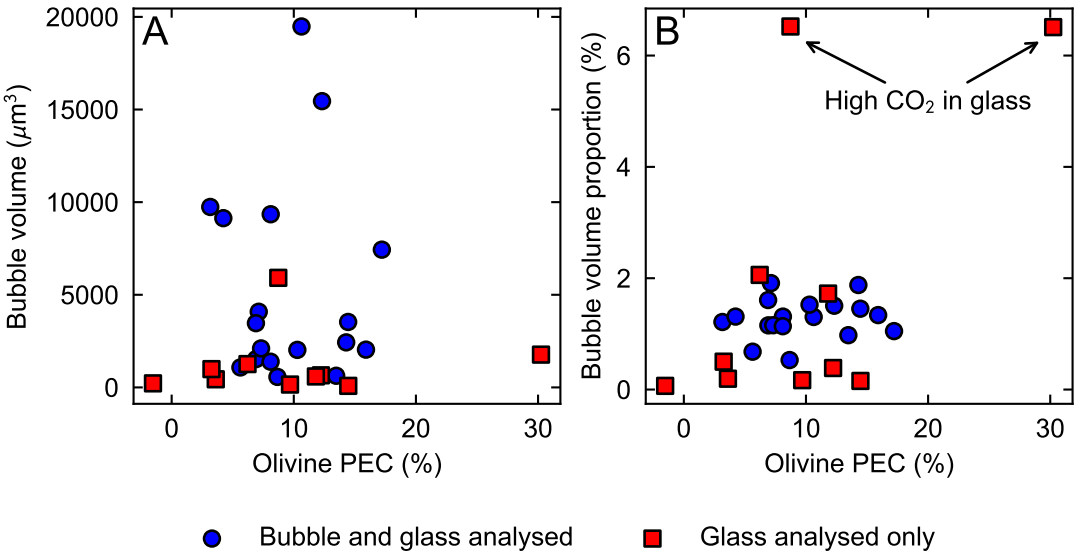

Figure S5. Olivine post-entrapment crystallization of analyzed melt inclusions plotted against A. bubble volume, and B. bubble volume as a proportion of the melt inclusion.

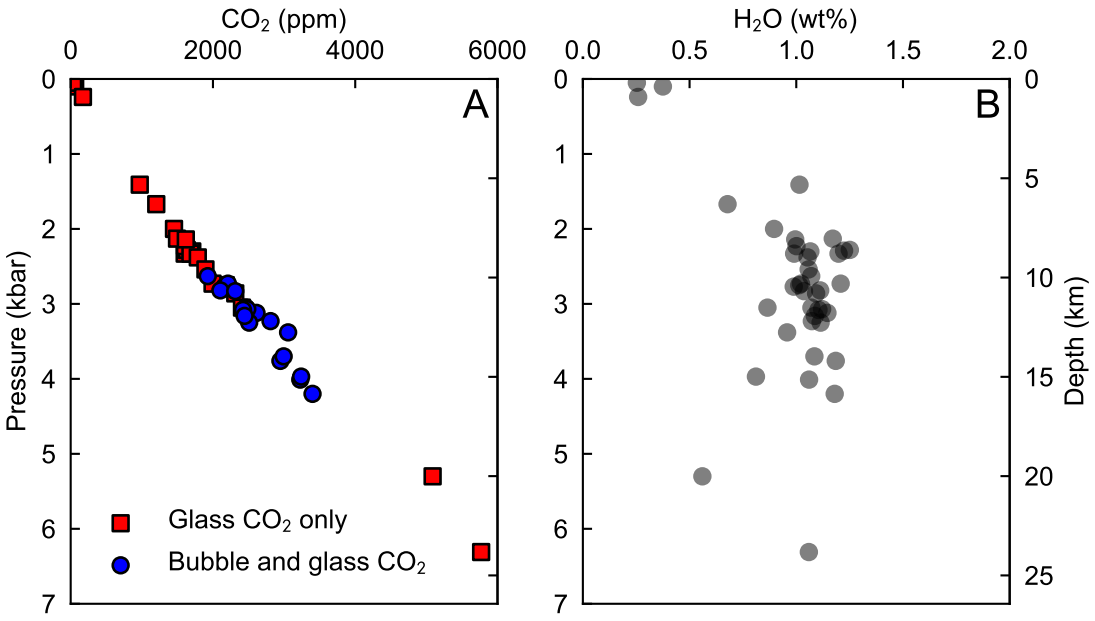

Figure S6. A) CO_2 and B) H_2O concentrations of MER melt inclusions plotted against volatile saturation pressures calculated using MagmaSat (Ghiorso & Gualda, 2015).

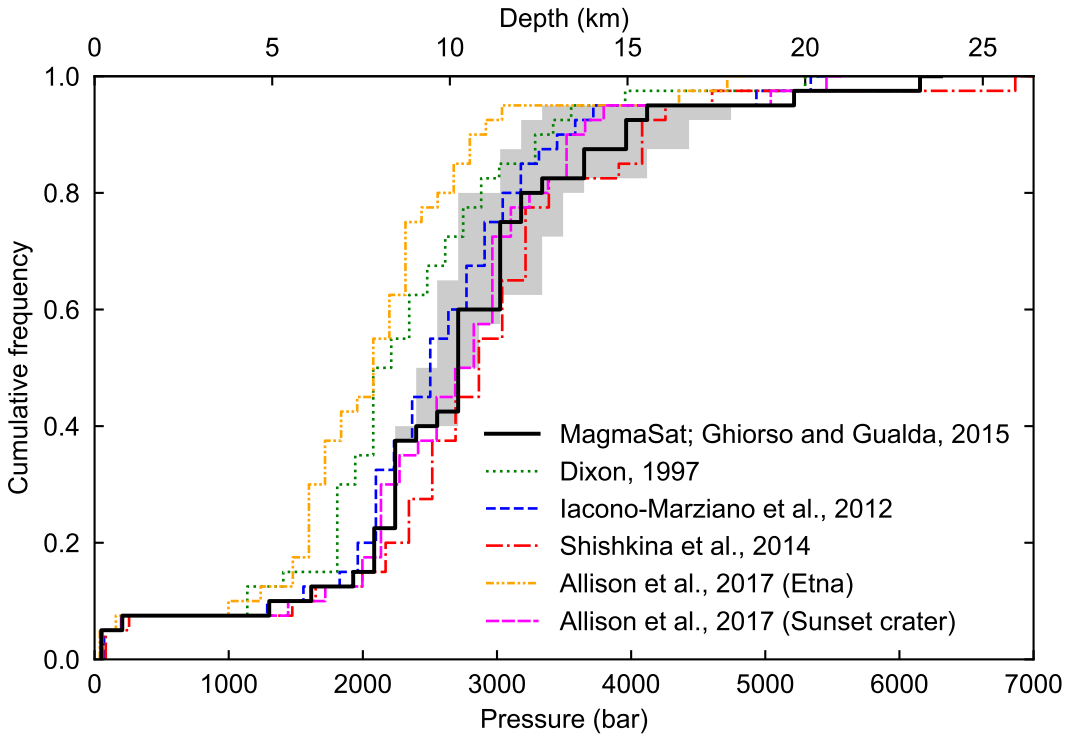

Figure S7. Cumulative distribution functions of entrapment pressures from different solubility models. The shaded region shows the error on MagmaSat entrapment pressures resulting from uncertainty in estimating bubble proportions from 2D images (Tucker et al., 2019).

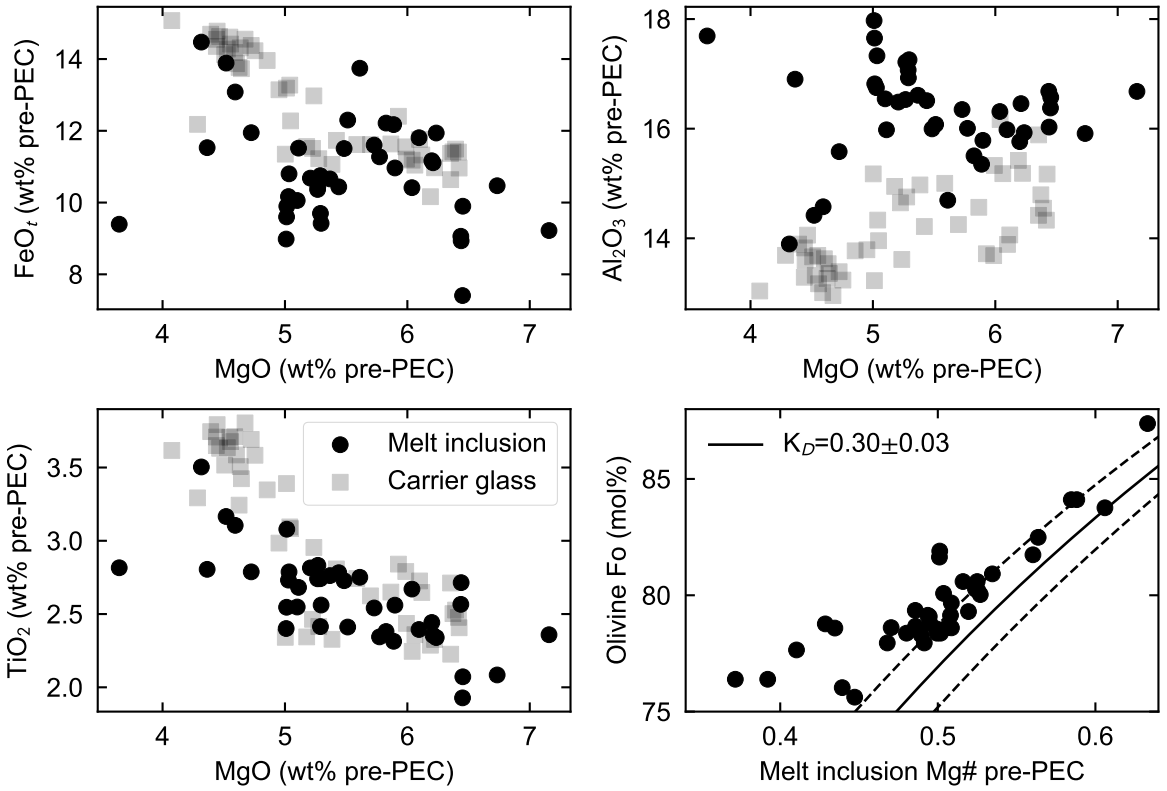

Figure S8. Melt inclusion major element geochemistry before post-entrapment crystallisation corrections. Carrier glass compositions are shown as the faded squares. Mg# is calculated as Mg/(Mg+Fe^{2+}), assuming 90 % of Fe is Fe^{2+}. Fo is calculated as in the caption to Figure 3 in the main text.

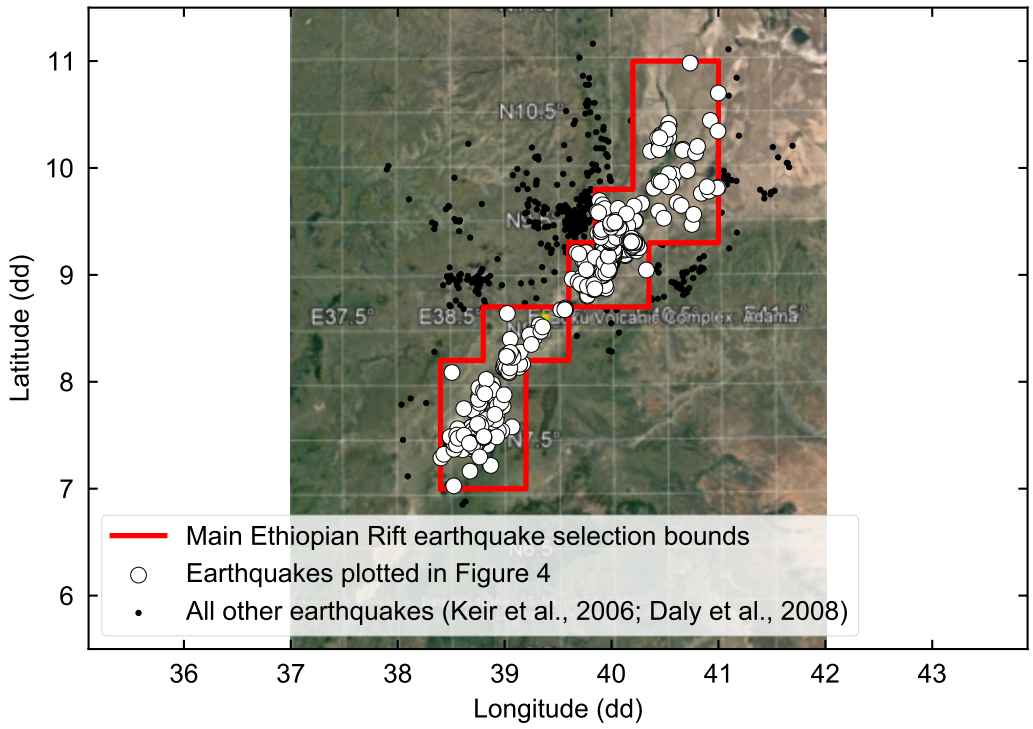

Figure S9. Earthquakes selected for earthquake histogram of Figure 4C in the main text. Areal limits are selected to encompass only earthquakes within the MER, and to avoid earthquakes that may be attributed to rift border fault seismicity. Earthquake data is from the EAGLE project (Keir et al., 2006; Daly et al., 2008).